



# Infant-phase reddening by surface Fe-peak elements in a normal type Ia supernova

Yuan Qi Ni <sup>1</sup>, Dae-Sik Moon <sup>1</sup>✉, Maria R. Drout <sup>1</sup>, Abigail Polin<sup>2,3</sup>, David J. Sand<sup>4</sup>, Santiago González-Gaitán <sup>5</sup>, Sang Chul Kim <sup>6,7</sup>, Youngdae Lee <sup>6,8</sup>, Hong Soo Park <sup>6,7</sup>, D. Andrew Howell<sup>9,10</sup>, Peter E. Nugent <sup>11,12</sup>, Anthony L. Piro<sup>2</sup>, Peter J. Brown<sup>13,14</sup>, Lluís Galbany <sup>15,16</sup>, Jamison Burke<sup>9,10</sup>, Daichi Hiramatsu <sup>9,10,17,18</sup>, Griffin Hosseinzadeh <sup>4</sup>, Stefano Valenti<sup>19</sup>, Niloufar Afsariardchi <sup>1</sup>, Jennifer E. Andrews<sup>4</sup>, John Antoniadis<sup>20,21,22</sup>, Iair Arcavi <sup>23,24</sup>, Rachael L. Beaton <sup>2,25,39,40</sup>, K. Azalee Bostroem <sup>26</sup>, Raymond G. Carlberg <sup>1</sup>, S. Bradley Cenko <sup>27,28</sup>, Sang-Mok Cha<sup>6,29</sup>, Yize Dong<sup>19</sup>, Avishay Gal-Yam <sup>30</sup>, Joshua Haislip<sup>31</sup>, Thomas W.-S. Holoien<sup>2</sup>, Sean D. Johnson <sup>25</sup>, Vladimir Kouprianov <sup>31,32</sup>, Yongseok Lee <sup>6,29</sup>, Christopher D. Matzner <sup>1</sup>, Nidia Morrell <sup>33</sup>, Curtis McCully<sup>9,10</sup>, Giuliano Pignata<sup>34,35</sup>, Daniel E. Reichart<sup>31</sup>, Jeffrey Rich<sup>2</sup>, Stuart D. Ryder <sup>36,37</sup>, Nathan Smith <sup>4</sup>, Samuel Wyatt<sup>4</sup> and Sheng Yang <sup>38</sup>

**Type Ia supernovae are thermonuclear explosions of white dwarf stars. They play a central role in the chemical evolution of the Universe and are an important measure of cosmological distances. However, outstanding questions remain about their origins. Despite extensive efforts to obtain natal information from their earliest signals, observations have thus far failed to identify how the majority of them explode. Here, we present infant-phase detections of SN 2018aoz from a very low brightness of  $-10.5$  AB absolute magnitude, revealing a hitherto unseen plateau in the  $B$  band that results in a rapid redward colour evolution between 1.0 and 12.4 hours after the estimated epoch of first light. The missing  $B$ -band flux is best explained by line-blanket absorption from Fe-peak elements in the outer 1% of the ejected mass. The observed  $B - V$  colour evolution of the supernova also matches the prediction from an over-density of Fe-peak elements in the same outer 1% of the ejected mass, whereas bluer colours are expected from a purely monotonic distribution of Fe-peak elements. The presence of excess nucleosynthetic material in the extreme outer layers of the ejecta points to enhanced surface nuclear burning or extended subsonic mixing processes in some normal type Ia SN explosions.**

Type Ia supernovae (SNe) are the main source of Fe-peak elements in the Universe<sup>1</sup>, and their use in measuring extragalactic distances led to the discovery of accelerated cosmological expansion and dark energy<sup>2,3</sup>. Despite their fundamental importance, the explosion mechanisms of type Ia SNe remain a matter of extensive debate<sup>4</sup>, particularly for the ‘normal’ events, which comprise  $\sim 70\%$  of their population<sup>5</sup>. Normal type Ia SNe may be ignited by nuclear burning in a white dwarf when binary accretion or merger causes its mass to reach the critical Chandrasekhar limit ( $\sim 1.4 M_{\odot}$ ). Alternatively, recent studies have shown that they may also arise from sub-Chandrasekhar-mass white dwarfs via a helium-shell double detonation (He-shell DDet), in which the detonation of a thin helium layer on the surface of the white dwarf subsequently ignites carbon in the core<sup>6–8</sup>. Normal type Ia SNe may arise from multiple explosion channels, and it is uncertain what fraction of them are produced by different explosion channels. It has been suggested that He-shell DDet can potentially account for up to  $\sim 40\%$  of them<sup>6</sup>.

Historically, most type Ia SNe are discovered and monitored around the peak of their light curves 2–3 weeks post-explosion, when their emission is dominated by the decay of  $^{56}\text{Ni}$  concentrated in the centre of their ejecta. However, multiple explosion processes, such as subsonic mixing<sup>9</sup> and surface He burning<sup>6,10</sup>, predict

over-densities of Fe-peak elements in the shallow outer layers of the ejecta, leading to excess emission and short-lived spectroscopic features in the faint and elusive ‘infant’ phase within a few days post-explosion. Excess red emission identified between 1 and 5 days in at least two spectroscopically peculiar events was interpreted to be from the ashes of a He-shell detonation<sup>11–13</sup>. On the other hand, multiple events from the normal<sup>14–17</sup> and overluminous<sup>18,19</sup> subtypes have been observed with excess blue emission until 5 days. There are several possible interpretations for the blue emission, including excess heating from a  $^{56}\text{Ni}$  over-density<sup>15,20</sup>. For the vast majority of type Ia SNe observed between 1 and 5 days, the rising parts of their light curves match simple power-law profiles<sup>21–26</sup>, consistent with a centrally concentrated and monotonic distribution of  $^{56}\text{Ni}$  under the ejecta surface. Overall, observations to date have tightened constraints on the distribution of nucleosynthetic elements in normal type Ia SNe, but how they explode remains uncertain<sup>13</sup>. Deep multicolour observations covering the infant phase within  $\sim 1$  day post-explosion can shed new light on this longstanding problem.

## Discovery and follow-up observations of SN 2018aoz

SN 2018aoz was first detected at 00h54m on 29 March 2018 Universal Time (UT) in a  $B$ -band image taken by the Korea Microlensing Telescope Network (KMTNet)<sup>27,28</sup> of a field containing

A full list of affiliations appears at the end of the paper.

the elliptical galaxy NGC 3923 (ref. <sup>29</sup>) at redshift  $z=0.00580$  (Table 1). Unlike in previous studies of type Ia SNe, our observations were obtained in three bands ( $B$ ,  $V$  and  $I$ ) from the moment of first detection, at an average cadence of 4.7 h. The first detections in the  $V$  and  $I$  bands followed 2 min and 2.4 h later, respectively, whereas it was not detected in images from the previous night. The source was also identified by the Distance Less Than 40 Mpc survey (DLT40)<sup>30</sup> 1.1 days after the first KMTNet detection, reported to the Transient Name Server at 07 h 25 m on 2 April 2018 UT, and classified as a normal type Ia SN with a spectrum obtained by the Las Cumbres Observatory<sup>31</sup> at 09 h 25 m on 2 April 2018 UT. The discovery triggered an extensive follow-up campaign in which ultraviolet, optical and near-infrared imaging and spectroscopy were performed.

Figure 1 compares part of our high-cadence  $UBVri$  light curves of SN 2018aoz (see Supplementary Information for the full ultraviolet to near-infrared light curves) with early light curves of other normal type Ia SNe after Galactic extinction correction (Methods). Note that the KMTNet  $BVI$ -band observations are calibrated to the nearest AAVSO (American Association of Variable Star Observers) standard filters ( $BVi$ ; see Methods). The  $B$ -band light curve peak absolute magnitude,  $M_{\max}(B) = -19.32$  mag, and decline rate over the first 15 days post-peak,  $\Delta M_{15}(B) = 1.12$  mag—two parameters commonly used to classify type Ia SNe<sup>32</sup>—identify SN 2018aoz as a normal type Ia. The early light curves of SN 2018aoz rise faster than most normal events such as SNe 2011fe<sup>21,33</sup>, 2018oh<sup>17,34</sup> and 2017cbv<sup>15,20</sup>, which have  $M_{\max}(B)$  and  $\Delta M_{15}(B)$  values similar to those of SN 2018aoz, although the total rest-frame rise time of SN 2018aoz from its onset to  $B$ -band maximum (15.32 days) is consistent with events near the lower extreme of the rise time distribution of the normal population (15–22 days<sup>26</sup>).

### Earliest observations: $B$ -band plateau and excess emission

The onset of the light curve (or ‘epoch of first light’) is estimated to be 23 h 54 m on 28 March 2018 UT (modified Julian date (MJD) 58205.9958), or  $1.0 \pm 0.5$  h before the first detection (see below), making it one of the earliest  $3\sigma$  detections for any type Ia SN. Figure 1 (inset) compares the earliest observations of SN 2018aoz to those of other normal type Ia SNe in filters nearest to the  $V$  band. The observations of SN 2018aoz over the first  $\sim 0.5$  days constitute some of the lowest luminosity signals ever detected from an early type Ia SN—up to a factor of 3 below the first detected luminosity of SN 2011fe<sup>21</sup>. In this unexplored ‘infant’ phase and depth, the  $B$ -band fluxes are nearly constant (the ‘ $B$ -band plateau’) whereas the  $Vi$  bands rise rapidly at a rate of  $\sim 2$  mag per day, resulting in an abrupt redward evolution of the  $B-V$  colour by 1.5 mag between 1.0 h and 12.4 h after first light (Fig. 2). These features have not yet been identified in other type Ia SNe.

To estimate the epoch of first light, we fit a power-law model to the rising light curves of SN 2018aoz (Supplementary Section 1), as typically adopted in the analysis of type Ia SNe<sup>11,17,21–26,35</sup>. The  $B$ -band light curve during 0–0.5 days was omitted from the fitting to avoid the uncertainty associated with the  $B$ -band plateau. Figure 3 (left panels) compares the best-fit power-law to the observed light curves of the SN over the fitting interval (0–7 days). In the infant phase of 0–0.5 days, faint excess emission over the simple power-law fit is evident in the  $V$  and  $i$  bands, simultaneous with the  $B$ -band plateau. In subsequent epochs, the power-law provides an acceptable fit to the rising light curves, consistent with the vast majority of type Ia SNe such as 2011fe (Fig. 1), whereas there is no evidence for excess emission in SN 2018aoz at the brightness level of the excess emission observed in SNe 2018oh and 2017cbv during 1–5 days.

### Origin of infant-phase emission in the extreme outer ejecta

The appearance of a short-duration  $B$ -band plateau and simultaneous excess emission over the power-law emission almost immediately following the SN explosion would localize the mechanisms

**Table 1 | Properties of SN 2018aoz**

Parameter	Value <sup>a</sup>
Sky coordinates (RA, dec.) (J2000)	(11 h 51 m 01.80 s, $-28^{\circ} 44' 38.48''$ )
Redshift of host galaxy NGC 3923 (ref. <sup>29</sup> ) ( $z$ )	$0.00580 \pm 0.00003$
First detection (UT, MJD)	00 h 54 m on 29 March 2018, MJD 58206.03779
Observed peak apparent magnitudes of $BVi$ -band light curves	12.81 mag ( $B$ ), 12.80 mag ( $V$ ), 13.26 mag ( $i$ )
Observed peak epochs of $BVi$ -band light curves	MJD 58221.41 ( $B$ ), 58221.30 ( $V$ ), 58218.29 ( $i$ )
Power-law indices of first light <sup>b</sup> ( $\alpha$ )	$2.24 \pm 0.02$ ( $B$ ), $1.99 \pm 0.02$ ( $V$ ), $2.26 \pm 0.01$ ( $i$ )
Epoch of first light <sup>b</sup> ( $t_{\text{eff}}$ )	MJD 58206.00 $\pm$ 0.02
Difference between epochs of first light and first detection	$1.0 \pm 0.5$ h
Post-peak decline rate <sup>c</sup> ( $\Delta M_{15}(B)$ )	$1.117 \pm 0.015$ mag
Colour stretch parameter <sup>c</sup> ( $s_{BVi}$ )	$0.797 \pm 0.019$
Peak absolute magnitudes <sup>c</sup>	$-19.32$ mag ( $B$ ), $-19.23$ mag ( $V$ ), $-18.61$ mag ( $i$ )
Peak Si II velocity <sup>d</sup>	$(11.43 \pm 0.12) \times 10^3$ km s <sup>-1</sup>
Explosion epoch <sup>e</sup> ( $t_{\text{exp}}$ )	MJD 58205.6 $\pm$ 0.7
Peak luminosity of bolometric light curve <sup>f</sup> ( $L_{\text{peak}}$ )	$1.42 \times 10^{43}$ erg s <sup>-1</sup>
Peak epoch of bolometric light curve <sup>f</sup>	$-1.16$ days
<sup>56</sup> Ni mass <sup>g</sup> ( $M_{\text{Ni}}$ )	$0.509 \pm 0.006 M_{\odot}$
$\tau_m$ parameter <sup>g</sup>	$9.51 \pm 0.26$ days
Ejecta mass <sup>g</sup> ( $M_{\text{ej}}$ )	$\sim 0.8$ – $1.0 M_{\odot}$
Ejecta kinetic energy <sup>g</sup> ( $E_{\text{ej}}$ )	$\sim (0.6$ – $0.8) \times 10^{51}$ erg

<sup>a</sup> All time and date values are given in the observer frame. <sup>b</sup> From the power-law fit to the  $BVi$ -band early light curves (Supplementary Section 1). <sup>c</sup> For the rest-frame  $BVi$ -band light curves (Methods). <sup>d</sup> See Supplementary Section 2. <sup>e</sup> From the power-law fit to the Si II velocity evolution (Supplementary Section 2). <sup>f</sup> See Supplementary Section 3. <sup>g</sup> From modelling the bolometric luminosity (Supplementary Section 4).

responsible for these features to the extreme outer ejecta where the optical depth is lower. However, the short 15.3-day rise time of SN 2018aoz compared to the 18.9-day average for normal type Ia SNe could, in principle, indicate a long ‘dark phase’ between the epochs of explosion and first light due to the time delay for radioactive photons to diffuse out of the ejecta<sup>36</sup>. To examine the presence of such a dark phase in SN 2018aoz, we estimate the explosion epoch,  $t_{\text{exp}}$ , by fitting its photospheric velocity evolution traced by the Si II  $\lambda 6355$  Å absorption feature with a power-law model that has provided a good fit to other type Ia SNe<sup>15,37</sup> (Supplementary Section 2), obtaining  $t_{\text{exp}} = \text{MJD } 58205.6 \pm 0.7$  (0.4 days prior to first light). As this method is independent of the distribution of radioactive photons, it is also dark-phase-independent. The difference between the epochs of explosion and first light constrains the dark phase in SN 2018aoz to be  $\lesssim 1$  day, disfavouring the dark phase explanation for its short rise time among normal events. Instead, the shorter rise time can be attributed to a smaller effective ejecta mass along the line of sight, or a smaller total ejecta mass assuming spherically symmetric ejecta (Supplementary Section 4).

The mass of material in the outer ejecta that is visible via photon diffusion at time  $t$  post-explosion,  $\Delta M(t)$ , can be estimated

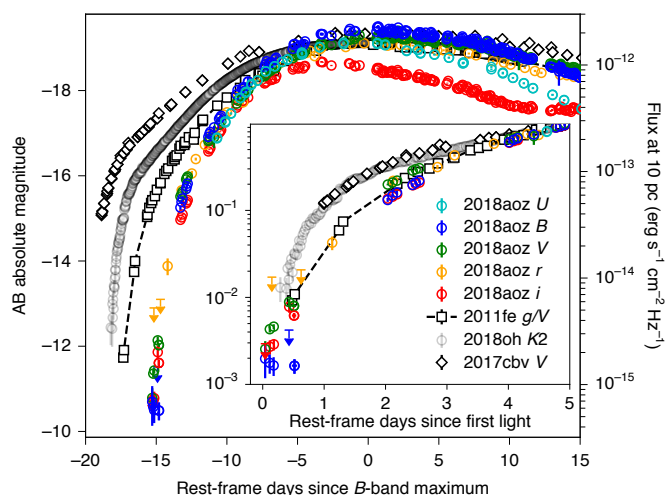


**Fig. 1 | Subset of the light curves of SN 2018aoz compared to three other early SNe.** The de-reddened  $UBVri$ -band early light curves of SN 2018aoz (coloured circles) are compared to those of normal type Ia SNe 2011fe<sup>70</sup>, 2018oh<sup>17</sup> and 2017cbv<sup>15</sup> in filters nearest to the V band. The error bars represent the  $1\sigma$  uncertainty level and the inverted arrows are  $3\sigma$  detection limits. The light curves of SN 2018aoz show a faster pre-peak rise than those of the other three SNe, although they have similar post-peak decline rates. The inset shows the early light curves of the SNe within 5 days of their epochs of first light, where excess emission has previously been identified in some type Ia SNe<sup>15,17,19</sup>, normalized to their luminosities at 5 days. SN 2018oh and 2017cbv both show excess emission between 1 and 5 days, whereas SN 2011fe shows a typical power-law-like rise. The light curves of SN 2018aoz after  $-0.5$  days are similar to that of SN 2011fe. Between 0 and 0.5 days the light curves of SN 2018aoz reveal the infant phase of type Ia SN evolution. In this phase, the  $B$ -band light curve stalls, showing a ‘plateau’ feature, whereas the  $Vi$ -band ones rise rapidly at a rate of  $\sim 2$  mag per day.

via the following equation derived from a polytropic ( $n=3$ ) ejecta profile expected for an exploding white dwarf undergoing homologous expansion<sup>36</sup>:

$$\Delta M \approx 2 \times 10^{-2} \left( \frac{\kappa}{0.1 \text{ cm}^2 \text{ g}^{-1}} \right)^{-0.88} \left( \frac{M_{\text{ej}}}{1.4 M_{\odot}} \right)^{-0.32} \left( \frac{E_{\text{ej}}}{10^{51} \text{ ergs}} \right)^{0.44} \left( \frac{t - t_{\text{exp}}}{1 \text{ day}} \right)^{1.76} M_{\odot}, \quad (1)$$

where  $M_{\text{ej}}$  and  $E_{\text{ej}}$  are the mass and kinetic energy of the SN ejecta, respectively, and  $\kappa \approx 0.1 \text{ cm}^2 \text{ g}^{-1}$  is expected for  $^{56}\text{Ni}$ -dominated opacity<sup>38</sup>. The equation can be rewritten compactly in terms of the parameter  $\tau_{\text{m}}$ , the geometric mean of the diffusion and expansion timescales:

$$\frac{\Delta M}{M_{\text{ej}}} \approx 1.3 \left( \frac{t - t_{\text{exp}}}{\tau_{\text{m}}} \right)^{1.76} M_{\odot}, \quad \tau_{\text{m}} = \left( \frac{\kappa}{13.8 c} \right)^{1/2} \left( \frac{6 M_{\text{ej}}^3}{5 E_{\text{ej}}} \right)^{1/4}. \quad (2)$$

Adopting  $\tau_{\text{m}}=9.5$  days from modelling the observed bolometric luminosity of the SN (Supplementary Sections 3 and 4), this locates the origin of the infant-phase features of SN 2018aoz visible  $\lesssim 1$  day post-explosion within the outer  $\sim 2\%$  of the SN-ejected mass along the line of sight.

### Origin of the infant-phase $B$ -band plateau and red $B - V$ colour

We examine whether the infant-phase  $B$ -band plateau and redward  $B - V$  colour evolution are consistent with blackbody

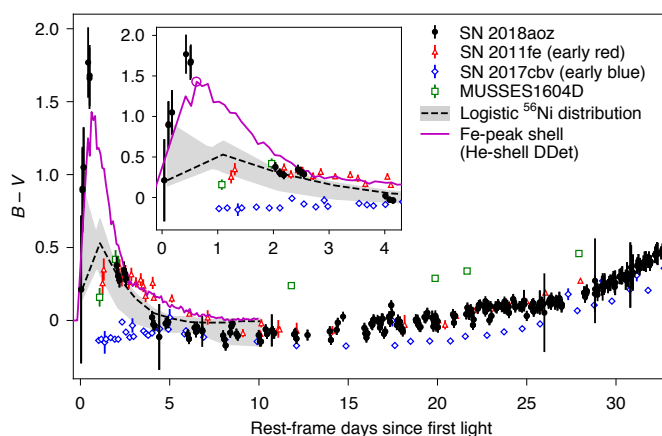


**Fig. 2 | Comparison of the colour evolution of SN 2018aoz to other SNe and models.** The de-reddened  $B - V$  colour of SN 2018aoz (black filled circles) is compared to those of normal type Ia SNe 2011fe<sup>70</sup> and 2017cbv<sup>15</sup> from the ‘early red’ and ‘early blue’ groups<sup>19</sup>, respectively, and that of MUSSES1604D<sup>11</sup>, a spectroscopically peculiar type Ia SN with an early redward colour evolution. The error bars represent the  $1\sigma$  uncertainty level. Also shown are colour curves of fitted models from radiative transfer calculations of two different  $^{56}\text{Ni}$  distributions: from a pure logistic  $^{56}\text{Ni}$  distribution (black dashed curve with grey shaded error region; see Supplementary Section 7.2), and a logistic-like  $^{56}\text{Ni}$  distribution with Fe-peak elements in the outer 1% of the SN-ejected mass (magenta solid curve) from a  $0.01 M_{\odot}$  He-shell +  $1.05 M_{\odot}$  white dwarf He-shell DDet simulation. The  $B - V$  colour of SN 2018aoz is obtained by linearly interpolating each of the  $BV$ -band light curves to the union of their epochs, whereas those of other SNe (2011fe, 2017cbv and MUSSES1604D) were obtained by binning each of their light curves with intervals of 0.05, 0.1 and 0.1 days, respectively, starting from their first observations. The inset zooms in on the period of 0–4 days, where SN 2018aoz shows an infant-phase redward colour evolution within the first  $-0.5$  days due to the  $B$ -band plateau. The colour evolution of SN 2018aoz after  $-0.5$  days is consistent with that of SN 2011fe and with the logistic  $^{56}\text{Ni}$  distribution. The magenta open circle shows the epoch of the simulated He-shell DDet spectrum in Fig. 4 (magenta spectrum).

emission from cooling shock interactions that can be readily expected in early type Ia SNe (for example, ejecta collision with a companion<sup>39</sup>). Figure 4 compares the observed spectral energy distribution (SED) of SN 2018aoz in  $BVi$  filters at 0.5 days, when the  $B - V$  colour peaks, to those of various blackbodies. Clearly, it is impossible to fit all three  $BVi$  bands at this epoch with a single blackbody distribution. The  $Vi$ -band fluxes alone are consistent with a  $13,000 \pm 5,000$  K blackbody, which is within the expectations for shock-heated SN ejecta<sup>39,40</sup>. However, accommodating the low  $B$ -band flux level requires either unreasonably cold temperatures for early type Ia SNe or a break in the spectrum between the  $B$  and  $V$  bands ( $\sim 5,000$  Å) with  $\gtrsim 70\%$  flux suppression bluewards of the break (Supplementary Section 6). This indicates that although the underlying emission may be thermal in origin, a suppression of the  $B$ -band flux relative to the blackbody distribution is required to reproduce the observed SED of SN 2018aoz during the infant phase. Note that continuous extinction (for example, by circumstellar dust) is unable to explain the suppression, even for the case of extreme dust extinction (Supplementary Section 6). For a photospheric radius of  $2.5 \times 10^{14}$  cm at 0.9 days post-explosion—estimated by adopting a polytropic ( $n=3$ ) ejecta profile<sup>36</sup> with  $\tau_{\text{m}}=9.5$  days and the observed Si II velocity near peak (Table 1) as the characteristic ejecta velocity—the amount of  $B$ -band flux suppression needed to explain the observed SED at

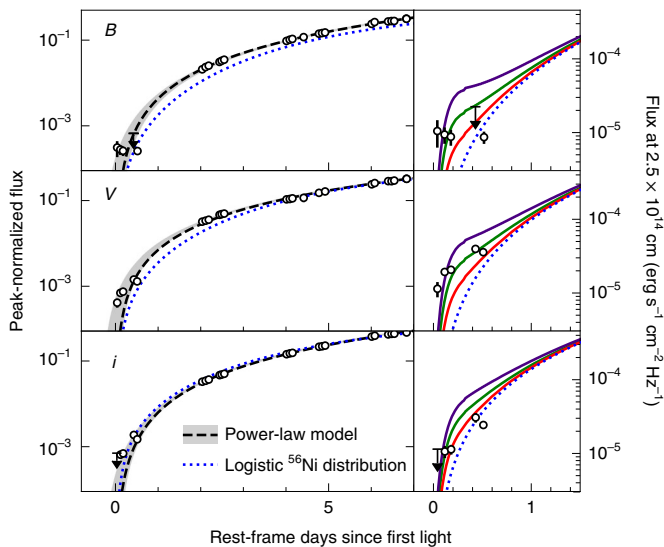


**Fig. 3 | Early light curves of SN 2018aoz compared to those of model predictions.** Left, the rest-frame de-reddened  $BVi$ -band (from top to bottom) light curves of SN 2018aoz (circles) are compared to the best-fit power-law (black dashed curve) and the best-fit blackbody light curve model powered by a logistic  $^{56}\text{Ni}$  distribution peaked at the ejecta core (blue dotted curve). The error bars of the data points represent the  $1\sigma$  uncertainty level and the inverted arrows are  $3\sigma$  detection limits. The upper and lower boundaries of the grey shaded region are the fitted power laws when the infant-phase data during 0–0.5 days are entirely excluded and included, respectively. Right, the observed infant-phase fluxes of SN 2018aoz before 0.5 days at its approximate photospheric radius are compared to the logistic  $^{56}\text{Ni}$  model (blue dotted curve), along with modified logistic  $^{56}\text{Ni}$  models (coloured curves) in which the total  $^{56}\text{Ni}$  mass in the outer 0.31% of the SN-ejected mass has been increased to  $(0.9, 1.8$  and  $3.6) \times 10^{-4} M_{\odot}$  (red, green and purple). The increases in  $^{56}\text{Ni}$  lead to excess emission before  $\sim 1$  day.

0.5 days is  $(3.2 \pm 0.6) \times 10^{-5} \text{ erg s}^{-1} \text{ cm}^{-2} \text{ Hz}^{-1}$  for a  $13,000 \pm 5,000 \text{ K}$  blackbody source, corresponding to an isotropic  $B$ -band energy deficit of  $(2.5 \pm 0.5) \times 10^{25} \text{ erg s}^{-1} \text{ Hz}^{-1}$ .

Such a selective suppression of flux can only be from line absorption. Fe-peak and associated nucleosynthetic elements, including  $^{56}\text{Ni}$ ,  $^{52}\text{Fe}$ ,  $^{48}\text{Cr}$ ,  $^{44}\text{Ti}$  and their decay products, are the elements expected in type Ia SNe that can substantially suppress flux in the vicinity of  $\lesssim 5,000 \text{ \AA}$ . Although H and He lines can blanket  $\lesssim 4,000 \text{ \AA}$  (refs. <sup>41,42</sup>), they are not generally expected in type Ia SNe and most of the  $B$ -band flux would not be affected. We find that a distribution of Fe-peak elements near the ejecta surface can reproduce the  $B$ -band suppression, offering the best explanation for the infant-phase  $B$ -band plateau and red  $B-V$  colour of SN 2018aoz. In Fig. 4, the observed SED at 0.5 days ( $\sim 0.9$  days post-explosion) is compared to the modelled spectrum of a type Ia SN with an excess of Fe-peak elements in the outer 1% of the SN-ejected mass at a nearly identical phase (1.05 days post-explosion), obtained by fitting the early light curves of SN 2018aoz with a grid of He-shell DDet simulations (see below). Indeed, the model predicts a  $\sim 5,000 \text{ \AA}$  spectroscopic break with substantial flux suppression bluewards of the break caused by Fe-line blanketing. Estimating the amount of suppression by performing photometry on the modelled spectrum using the KMTNet filters (Fig. 4, top panel), we obtain an isotropic  $B$ -band energy deficit of  $2.1 \times 10^{25} \text{ erg s}^{-1} \text{ Hz}^{-1}$  relative to the  $Vi$ -band continuum of the model, consistent with what is required to explain the infant-phase SED of SN 2018aoz.

### Distribution of Fe-peak elements in the extreme outer ejecta

To understand the origin of Fe-peak elements near the ejecta surface in SN 2018aoz, we investigate whether the elements are part of the centrally concentrated and monotonic main distribution of  $^{56}\text{Ni}$  in the ejecta or whether they constitute a distinct radial over-density in a shell (or clump, depending on the three-dimensional distribution). We find that the early light curves of the SN accommodate the presence of a radioactive shell or clump as follows. Figure 3 compares the observed early light curves to those predicted by blackbody models powered by four  $^{56}\text{Ni}$  distributions: a logistic function<sup>37</sup> peaked at the ejecta core fitted to the SN light curves during 0–10 days (Supplementary Section 5), representing the main  $^{56}\text{Ni}$  distribution, and the same function with total  $^{56}\text{Ni}$  mass in the outer 0.31% of the SN-ejected mass increased to  $(0.9, 1.8$  and  $3.6) \times 10^{-4} M_{\odot}$ . During 1–7 days, the logistic model follows rising behaviour similar to that of the SN luminosity, confirming that the  $^{56}\text{Ni}$  distribution is mainly centrally concentrated and monotonic under the ejecta surface. In the infant phase between 0 and 1 days, however, the pure logistic model underpredicts the observed luminosity in all three  $BVi$  bands. Excess radioactive materials is one possible explanation for the luminosity difference, as shown by the models with increased  $^{56}\text{Ni}$  fractions.

The stratification of Fe-peak elements in the ejecta also affects the  $B-V$  colour of the SN<sup>6,43</sup> as their absorption features (Fig. 4) evolve over time. Figure 2 shows that the  $B-V$  colour evolution of SN 2018aoz is best explained if the ejecta possesses an over-density of surface Fe-peak elements in addition to a centrally concentrated and monotonic  $^{56}\text{Ni}$  distribution. The observed colour curve is compared to those predicted by radiative transfer calculations of two different ejecta profiles: a purely logistic  $^{56}\text{Ni}$  distribution<sup>43</sup> fitted to the light curves of SN 2018aoz during 1–10 days (Supplementary Section 7.2), and a logistic-like  $^{56}\text{Ni}$  distribution with a shell of Fe-peak elements in the outer 1% of the ejected mass from the best-fit He-shell DDet simulation (see below). The model with an Fe-peak shell provides a much better fit to the observed colour evolution from the infant phase to later epochs than the one with a logistic distribution alone, although both models are consistent with the observed colour evolution after  $\sim 2$  days.

### Nature of SN 2018aoz and implications for type Ia SN origins

The presence of an Fe-peak shell or clump near the ejecta surface, as found in SN 2018aoz, has critical implications for the normal type Ia explosion mechanism. Simulations of type Ia SNe have shown that over-densities of Fe-peak elements in the extreme outer ejecta can result from either mixing during a subsonic explosion process or surface nuclear burning during the explosion. The former is predicted by some Chandrasekhar-mass explosion models, in which a white dwarf initially deflagrates subsonically before transitioning into a detonation<sup>9</sup>. When the explosion is spherically symmetric, the deflagration phase is usually limited to the inner ejecta, whereas a detonation is required to traverse the low-density outer ejecta<sup>44</sup>, a process that is not expected to produce surface Fe-peak clumps<sup>45</sup>. However, some simulations have found that asymmetric explosions resulting from off-centre deflagrations can produce surface Fe-peak clumps that are visible from a limited set of favourable viewing angles<sup>45,46</sup>, which could be one possible explanation for the distribution of Fe-peak elements in SN 2018aoz. Separately, a gravitationally confined detonation, where the off-centre deflagration plume rises buoyantly to the progenitor surface, is another scenario that produces a spherical shell of Fe-peak elements near the ejecta surface, although recent simulations have shown that this produces peculiar explosions that are incompatible with normal type Ia SNe<sup>47</sup>.

Sub-Chandrasekhar-mass He-shell DDet offer another way to produce Fe-peak elements in the outer ejecta. In the case of the spectroscopically peculiar type Ia SN MUSSES1604D<sup>11</sup>, the detonation of a  $0.054 M_{\odot}$  He-shell was invoked to explain its redward colour

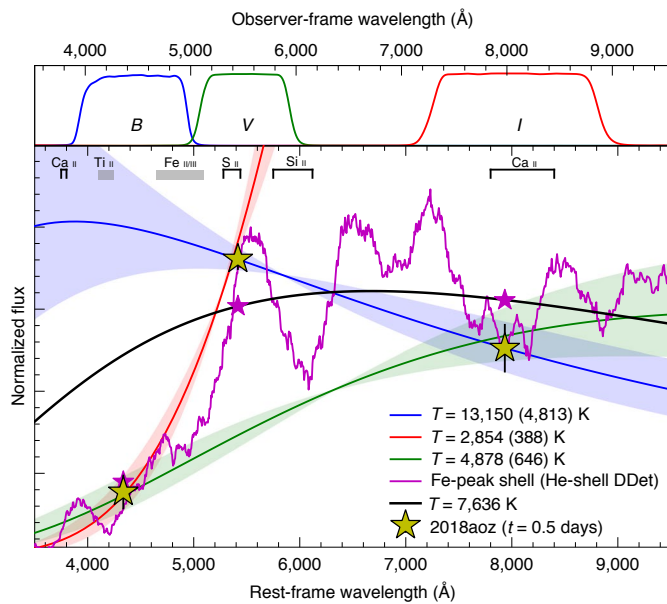


**Fig. 4 | Infant-phase SED of SN 2018aoz compared to model predictions.**

Top, the KMTNet *BVi* transmission curves used for *BVi* photometry. Bottom, the de-reddened *BVi* fluxes of SN 2018aoz (yellow stars) at 0.5 days (0.9 days post-explosion), when the *B*-band suppression relative to the *Vi*-band flux is maximal, are compared to three cases. First, blackbody distributions (coloured curves with shaded  $1\sigma$  error regions) fitting the *B*–*V* (red), *V*–*i* (blue) and *B*–*i* (green) colours whose temperatures (*T*) are provided in the legend with  $1\sigma$  uncertainties in parentheses. Second, simulated spectrum (magenta) of a  $0.01 M_{\odot}$  He-shell +  $1.05 M_{\odot}$  white dwarf He-shell DDet from 1.05 days post-explosion with Fe-peak elements in the outer 1% of the SN-ejected mass (notable absorption features are labelled at the top of the panel). Third, a blackbody (black curve) compatible with the *Vi*-band fluxes of the simulated He-shell DDet spectrum (magenta stars) evaluated using the KMTNet transmission curves. The SN fluxes are from  $>7\sigma$  detections and their error bars represent  $1\sigma$  uncertainties. The magenta spectrum shows how a shell of Fe-peak elements near the ejecta surface can lead to selective *B*-band suppression in the infant phase.

evolution during 1–2 days post-explosion (Fig. 2). To investigate whether this scenario can explain a redward colour evolution with a much shorter timescale and larger amplitude, as observed in SN 2018aoz, we perform a grid of He-shell DDet type Ia SN simulations with a range of white dwarf and He-shell masses (Supplementary Section 7.1), fitting the observed light curves during 0–8 days. We obtain the best fit with a small He-shell mass of  $0.01 M_{\odot}$  on a  $1.05 M_{\odot}$  white dwarf, which also provides the best match to the near-peak *BVi* light curves and spectroscopic features. As shown above, this model can indeed explain the *B*-band suppression (Fig. 4, magenta spectrum) and *B*–*V* colour evolution (Fig. 2, magenta curve) of SN 2018aoz. If He-shell DDet is the origin of surface Fe-peak elements in SN 2018aoz, it would imply that detonations of He shells as thin as  $\sim 0.01 M_{\odot}$  can successfully initiate normal type Ia SNe, consistent with the predictions of our simulations and other recent simulations<sup>7,48</sup>. In our best-fit He-shell DDet model for SN 2018aoz, 12.9% of the outer 1% of the ejecta by mass is composed of  $^{56}\text{Ni}$ ,  $^{52}\text{Fe}$  and  $^{48}\text{Cr}$ . Although this is comparable to the amount of radioactive material needed to reproduce the infant-phase excess emission in SN 2018aoz (see ‘Distribution of Fe-peak elements in the extreme outer ejecta’), the He-shell DDet model underpredicts the emission in the  $\lesssim 0.5$  day time period (Supplementary Section 7.1), indicating that either the current He-shell DDet models do not fully capture

radioactive heating at early times or another source of emission is also required (for example, ejecta collision with a companion<sup>49</sup>). Future modelling is necessary to ascertain how the inclusion of more detailed effects would influence the inferred mass of surface Fe-peak elements in SN 2018aoz.

No other type Ia SN has been detected in multiple bands at early enough epochs and sufficient depth to identify the remarkable *B*-band plateau and extreme redward *B*–*V* colour evolution observed during the first  $\sim 1$  day post-explosion in SN 2018aoz. Thus, such features could be present in many normal type Ia SNe, but likely not all of them. Observationally, based on the colour evolution in later epochs (2–5 days; see Fig. 2), SN 2018aoz appears to belong to the ‘early red’ population of type Ia<sup>19</sup>, which comprises just over half of the normal events, although whether the reported ‘early red/blue’ dichotomy of type Ia SNe truly represents separate populations is still uncertain<sup>13,19,50</sup>. Theoretically, we note that two of the three type Ia SN explosion mechanisms described above that can accommodate the presence of surface Fe-peak elements can account for only some fractions of the entire normal type Ia population in current models: He-shell DDet leave almost no unburnt carbon, incompatible with  $>40\%$  of type Ia SNe<sup>51</sup>, and the strong asymmetry of the gravitationally confined detonation scenario leaves only a small (if existent) set of compatible viewing angles for normal events<sup>47</sup>. SN 2018aoz provides evidence that surface Fe-peak elements are required in at least a fraction of normal type Ia SN explosions.

## Methods

**Discovery and photometric observations of SN 2018aoz.** SN 2018aoz was identified by both the KSP<sup>27,52,53</sup> and the DLT40<sup>50</sup>. KSP uses the three 1.6 m telescopes of the KMTNet in Chile, South Africa and Australia to conduct a survey optimized for detecting and continuously monitoring infant SNe in multiple colours. Each telescope of the network is equipped with an identical wide-field charge-coupled device (WFCCD) camera with a field of view over four square degrees and with multiple filters. Between February and July 2018, we conducted high-cadence monitoring of a  $2^{\circ} \times 2^{\circ}$  field containing the nearby elliptical galaxy NGC 3923. We obtained  $\sim 700$  images of the field with 60 s exposure times at a mean cadence of 4.7 h in each of the *BVi* bands. (Note that the *I*-band observations are calibrated to AAVSO *i*-band magnitudes as described in ‘Photometric calibration’ below.) The typical limiting magnitude for a point source in these images is 21–22 mag at a signal-to-noise ratio (S/N) of 3. DLT40 uses the 0.4 m PROMPT5 telescope<sup>54</sup> at Cerro Tololo Observatory in Chile to conduct a daily cadence survey of nearby galaxies, also optimized for detecting SNe at an early phase. The survey observations are unfiltered with a typical single-epoch depth of 19–20 mag.

The earliest detections (S/N  $> 3$ ) of SN 2018aoz were made by KSP at 00 h 54 m on 29 March 2018 UT (MJD 58206.0378) in the *B* and *V* bands obtained with the Chilean KMTNet telescope at the coordinate (RA, dec.) = (11 h 51 m 01.80 s,  $-28^{\circ} 44' 38.5''$ ) (J2000), 3.72' away from the centre of NGC 3923 in the northern direction. Supplementary Fig. 1 (column 2) shows the first *BVi*-band images, taken within 4 min of each other, obtaining S/N values of 3.5, 4.3 and 1.9, respectively, at the source position. The apparent magnitudes of the source in the images were measured to be  $21.57 \pm 0.44$  mag,  $21.26 \pm 0.25$  mag and  $21.97 \pm 0.58$  mag, respectively, where the error includes contributions from background noise at the source position, from photometric calibration and from *B*-band S-correction (see below). The source was not detected in *B*-, *V*- or *I*-band images obtained 1.1 days before the first detection. DLT40 detected the source 1.1 days later and made the discovery report at 07 h 25 m on 2 April 2018 UT (MJD 58210.4158)<sup>55,56</sup>.

In addition to observations made by KSP and DLT40, we conducted optical photometric observations of SN 2018aoz using 1 m telescopes of the Las Cumbres Observatory (LCO) network of robotic telescopes in conjunction with the Global SN Project between 4.4 and 64 days since first light.<sup>31</sup> These observations are supplemented by ultraviolet observations acquired by the Neil Gehrels Swift Observatory<sup>57</sup> Ultra-Violet Optical Telescope (UVOT)<sup>58</sup> and by near-infrared observations from the ANDICAM<sup>59</sup> instrument on the SMARTS 1.3 m telescope at Cerro Tololo Observatory. The Swift-UVOT and ANDICAM observations were carried out during the periods of 5.5–59 and 9.1–110 days since first light, respectively.

**Photometric calibration.** Point-spread function (PSF) photometry of SN 2018aoz on KSP images was performed using the SuperNova Analysis Package (SNAP), a custom python-based pipeline for SN photometry and analysis. A local PSF was obtained by fitting a Moffat function<sup>60,61</sup> to nearby reference stars and

simultaneously fitting sky background emission with a first-order polynomial function. The fluxes of SN 2018aaz were obtained by fitting the local PSF near the source location, and the detection S/N is equal to the best-fit flux divided by its  $1\sigma$  uncertainty. Photometric flux calibration was performed against 6–9 standard reference stars within  $10'$  of the source from the AAVSO Photometric All-Sky Survey (APASS)<sup>62</sup> database whose apparent magnitudes are in the range of 15–16 mag; the observations in the *BVI* KMTNet filters were calibrated against reference stars in the nearest AAVSO filters (Johnson *BV* and Sloan *i'*, or *BVi*).

The KSP instrumental magnitudes for the AAVSO reference stars were transformed to standard *BVi* magnitudes using the equations from ref.<sup>63</sup>. However, the spectra of SNe, particularly after the peak, are notably different from the AAVSO standard stars used to derive the transformation equations. To account for this, we applied spectrophotometric (*S*)-corrections, which are magnitude corrections between instrument and standard filters derived by performing synthetic photometry on spectra obtained at the same epoch<sup>64</sup>. We applied interpolated *S*-corrections to observations following the first spectrum taken at UT 09 h 22 m on 2 April 2018 (MJD 58210.39), 4.4 days since first light. At epochs observed before 4.4 days, we applied the ref.<sup>63</sup> transformation equations to the source in lieu of *S*-corrections under the assumption that the spectrum of SN 2018aaz in the early phase is dominated by continuum emission, which is supported by the small magnitude of *S*-corrections before the peak.

We searched for faint background sources around the location of the SN by using  $\geq 300$  individual pre-SN images in each of the *BVI* bands to create the deep stacked images shown in Supplementary Fig. 2 (right panels). As seen in the figure, we identified a background source  $\sim 0.8''$  northeast of the SN position with apparent *BVi*-band magnitudes of  $24.90 \pm 0.27$  mag,  $24.02 \pm 0.20$  mag and  $22.39 \pm 0.08$  mag, respectively. (See ‘Host, distance and extinction’ below for the discussion of the nature of this source). In the *B* and *V* bands, the brightness of the source is substantially below the  $1\sigma$  detection limits of the earliest images within 0.5 days (22.9 mag and 22.7 mag for *B*-band and *V*-band detection images, respectively) and much smaller than that of the SN at any epoch ( $< 21.8$  mag for *B* band and  $< 21.3$  mag for *V* band). Therefore, we ignore the background source in the *B*-band and *V*-band photometry as it is incapable of meaningfully affecting the PSF photometry of SN 2018aaz. For the *i*-band photometry, we remove the background source when the SN brightness is  $\leq 100$  times that of the background source (which is only for epochs before  $\sim 0.5$  days) by measuring the SN flux using a Kron aperture containing both sources and subtracting the known flux of the background source.

Unfiltered observations obtained with the DLT40 survey were template-subtracted and then calibrated to APASS *r*-band observations of field stars. Additional optical observations with the LCO 1 m telescopes were carried out in the *U*, *B*, *V*, *g*, *r* and *i* bands. Photometric reduction for the LCO images was accomplished using ‘lcoogsnpipe’<sup>65</sup>, a PyRAF-based pipeline. Zeropoints for images in Landolt filters were calculated from Landolt standard field images taken by the telescopes on the same nights as the observations. Zeropoints for images in Sloan filters were calculated using APASS stars in the same field of view as SN 2018aaz.

Observations with the Neil Gehrels Swift Observatory were triggered under the Swift Guest Investigator key project ‘Swift Response to Nearby Supernovae’. Swift observations began at 13 h 57 m on 3 April 2018 UT (MJD 58211.5811) and used all six medium band filters, namely *UVW2*, *UVM2*, *UVW1*, *U*, *B* and *V*. Co-addition of same-day images and photometry were done using the pipeline of the Swift Optical Ultraviolet Supernova Archive (SOUSA)<sup>66</sup> and the photometry is calibrated to the UVOT Vega system<sup>67</sup>. The Swift/UVOT photometric reduction includes the subtraction of the host galaxy count rates using images obtained in August 2019. The UVOT photometry uses the September 2020 update to the time-dependent sensitivity correction<sup>68</sup>.

Seventeen epochs of *J*-, *H*- and/or *K*-band observations of SN 2018aaz were obtained with ANDICAM mounted to the 1.3 m telescope at the Cerro Tololo Inter-American Observatory (CTIO) and operated by the SMARTS Consortium under programme NAO-18A-0047. For each epoch, a set of 10 individual 20 s images were taken per band, with a hexagonal seven-position dithering of around 20 arcsec. The dithered frames were stacked to produce the final co-added images for each epoch. PSF photometry was performed on the SN and nearby field stars using standard ‘daophot’ packages within the Image Reduction and Analysis Facility (IRAF) software, and absolute calibration was performed using Two Micron All Sky Survey (2MASS)<sup>69</sup> *JHK* magnitudes.

The light curves of the SN from all the photometric observations are shown in Supplementary Fig. 3 and provided in Supplementary Table 1. The photometry will also be publicly available on the Open SN Catalog<sup>70</sup>.

**Robustness of infant-phase KSP photometry.** Supplementary Fig. 1 presents the *B*-, *V*- and *I*-band stamp images (rows 2–4) showing the detection of the source at the epoch of the first detection (column 2), three following epochs during its infant phase ( $\leq 0.5$  days since first light, columns 3–5) and one epoch immediately before and after the infant phase (columns 1 and 6, respectively), as well as a table (row 1) showing the time and moon position at each observation. The moon was nearly full and at 25–45° elevation during the epochs, contributing to the background noise in the images. We find *B*-band  $3\sigma$  detection limits of 20.8–21.9 mag in single-epoch images from 0–0.5 days, consistent with typical limiting magnitudes

for the KMTNet<sup>71</sup> and substantially deeper than the *B*-band plateau at multiple epochs in the phase, despite the moon brightness. Note that these limiting magnitudes are estimated in a conservative way from background pixel variations, which gives limits that are slightly shallower than the depths detectable using PSF photometry in our data. Supplementary Fig. 1 provides the measured S/N at the SN position in the bottom-right corner of each stamp image, showing the robust ( $S/N > 5$ ) detection of the SN in all three bands at 0.11 days, 0.18 days and 0.51 days during its *B*-band plateau and redward *B*–*V* colour evolution.

We confirm the detection of the infant-phase *B*-band suppression as follows. Supplementary Fig. 1 (column 5) shows stamp images of the SN at 0.51 days, when its *B*-band flux was lowest compared to the *V* and *i* bands and when its *B*–*V* colour reached maximum. The images were obtained by binning 2–3 adjacent images within 1.5 h of each other for higher S/N. Each of the *B*-, *V*- and *I*-band images robustly detected the SN with  $S/N > 7$ . In these images, we measure *BVi* magnitudes of the SN to be  $21.78 \pm 0.21$  mag,  $20.02 \pm 0.04$  mag and  $20.33 \pm 0.08$  mag, respectively, corresponding to a *B*-band flux that is  $3.7 \pm 0.7$  times lower than the average of the *V* and *i* bands, after applying extinction correction. The detection of the *B*-band suppression is also confirmed with synchronous *BVi* fluxes of the SN at 0.5 days (Fig. 4, yellow stars) obtained via Gaussian process light curve interpolation (see below), which show a *B*-band flux that is  $4.4 \pm 1.2$  times lower than the average of the *V* and *I* bands. We note that it is impossible to reconcile this difference with a modification to the flux of the background source located  $\sim 0.8''$  from the position of SN 2018aaz. The background source is 18 times dimmer than the SN at this epoch in *B* band and incapable of affecting the SN brightness meaningfully even if it vanished. Conversely, the background source brightness would have needed to increase by factors of 31 and 5.5 in the *V* and *I* bands, respectively, relative to its brightness in our deep stacked images, without a corresponding increase in the *B* band, to lower the inferred *V*- and *i*-band fluxes of the SN at this epoch to that of the *B* band. This is not supported by the centroids of the *V*- and *I*-band SN detections at this epoch, which are aligned with the SN position ( $< 0.04''$  away). We therefore conclude that the measured suppression of the *B*-band flux relative to that of the *V* and *I* bands is robust.

**Spectroscopy of SN 2018aaz.** We obtained 25 low-resolution optical spectra of SN 2018aaz spanning 4.4–136.3 days since first light with a combination of the Gemini Multi-Object Spectrograph (GMOS)<sup>72</sup> on the 8.1 m Gemini South telescope, the WFCCD on the 2.5 m du Pont telescope at Las Campanas Observatory, and the FLOYDS spectrographs located on the 2 m Faulkes telescopes of the Las Cumbres Observatory in Siding Spring and Haleakala<sup>31</sup>. Two moderate-resolution spectra were obtained near maximum light in the region around Na I D with the Blue Channel Spectrograph<sup>73</sup> on the MMT telescope. The spectroscopic observations are summarized in Supplementary Table 2.

Spectra from the du Pont and MMT telescopes were reduced using standard tasks within IRAF. Bias and flat-field corrections were performed on the two-dimensional frames, one-dimensional spectra were extracted and wavelength calibration was performed using calibration lamps taken immediately after target exposures. Flux calibration and telluric corrections were performed with a set of custom IDL scripts<sup>5,74</sup> using spectrophotometric standards observed on the same night. GMOS spectra were reduced in a similar manner, but using the custom ‘gmos’ suite of IRAF tasks. Initial flux calibration for GMOS spectra was performed using the IRAF tasks ‘standard’ and ‘calibrate’, and final scaling was performed based on matching to observed photometry.

A selection of our best low-resolution spectra are presented in Supplementary Fig. 4 (left panel), as well as the two moderate-resolution spectra. (The full set of spectra obtained will be available on the Open SN Catalog<sup>70</sup> and WISEREP<sup>75</sup>). As seen in the figure, the spectra of SN 2018aaz are dominated by high-velocity absorption features of Ca II, Fe II/III, Si II and Si II at early times. In particular, the presence of silicon features and the absence of hydrogen features confirm its type Ia SN nature. Supplementary Fig. 4 (top-right panel) shows that the spectrum of the SN near peak is nearly identical to normal type Ia SNe 1994D<sup>76</sup> and 2002dj<sup>77</sup>.

**Host, distance and extinction.** The host galaxy of SN 2018aaz is NGC 3923, an elliptical galaxy (Supplementary Fig. 2, left panel), as confirmed below by their matching redshifts and distance moduli. Using SNID<sup>78</sup>, we find a best-fit spectral template to the maximum light spectra of SN 2018aaz with a spectroscopic redshift of  $z = 0.0058 \pm 0.0007$ , which matches the known redshift of the galaxy<sup>79</sup>,  $z = 0.00580 \pm 0.00003$ . Using NED<sup>79</sup>, we determine a distance modulus, DM, of  $31.75 \pm 0.15$  mag to the SN based on Hubble flow in the cosmology of ref.<sup>80</sup> with corrections for peculiar velocities due to the Virgo Supercluster, Great Attractor and Shapley Supercluster<sup>81</sup>. This value is consistent with redshift-independent distances to NGC 3923 based on surface brightness fluctuations ( $DM = 31.64 \pm 0.14$  mag)<sup>82</sup> and to SN 2018aaz based on type Ia SN template fitting ( $DM = 31.75 \pm 0.08$  mag; see next section). The luminosity distance to the SN based on the type Ia SN template DM is  $22.4 \pm 0.8$  Mpc. The location of the SN  $\approx 3.72'$  north of the galaxy centre (Supplementary Fig. 2), corresponding to a projected distance of  $24.0 \pm 0.9$  kpc, places it in the stellar halo of the galaxy.

SN 2018aaz suffers from relatively little Galactic extinction as it is located near the Galactic south pole with  $E(B - V) = 0.093$  mag in its direction according to the extinction model of Schlafly & Finkbeiner<sup>83</sup>, corresponding

to extinction corrections of 0.40 mag, 0.29 mag and 0.18 mag for the  $B$ ,  $V$  and  $i$  bands, respectively, for an  $R_V = 3.1$  Fitzpatrick reddening law<sup>84</sup>. For the spectra and spectral energy distribution of the SN (Supplementary Information), we adopted Galactic extinction corrections based on the updated reddening law of Fitzpatrick & Massa<sup>85</sup>, which is slightly better in the ultraviolet regime. Given the halo environment of SN 2018aoz, little extragalactic extinction from NGC 3923 is expected. This is confirmed by the lack of observed Na I doublet (Na I D, 5,890 Å and 5,896 Å) absorption features at the redshift of the SN in two moderate-resolution MMT spectra (Supplementary Fig. 2, inset). We confirm the Galactic extinction to the source by fitting the equivalent widths of the Na I D in the observer frame using a Voigt doublet profile in each of the two MMT spectra<sup>86</sup>. The mean of the measurements is  $E(B - V) = 0.07 \pm 0.01$  mag, consistent with the value from Schlafly & Finkbeiner<sup>83</sup>. The non-detection of Na I D in the rest frame of the SN in these spectra constrains the host galaxy extinction to be substantially below this value. By scaling the measured Voigt profiles of the Galactic Na I D to the MMT spectra at  $z = 0.0058$ , we estimate a  $3\sigma$  upper limit on the equivalent width of Na I D of 0.11 Å, corresponding to  $E(B - V) < 0.02$  for the host galaxy, assuming a Milky-Way-like correlation between Na I D and dust extinction<sup>86</sup>.

The nature of the background source located  $\sim 0.8''$  northeast and underlying the position of SN 2018aoz in KSP images (Supplementary Fig. 2) is uncertain, although we consider several possibilities. It can be a source at the redshift of the SN, in which case the low  $V$ -band luminosity ( $-7.7$  mag) and red  $V - I$  colour ( $-1.6$  mag) of the source are consistent with it being a dwarf galaxy or globular cluster in NGC 3923 (refs. 87–89). The projected distance of  $\sim 86$  pc between the SN and the source in the rest frame opens the possibility for association between the two, although the source apparently does not provide a dusty host environment, as evidenced by the lack of Na I D lines in the rest frame (see above). Alternatively, the source can be a spatially coincident foreground star or background galaxy. Additional observations with higher spatial resolution are required to determine whether the source is separated from the SN or truly underlying it.

**Light curve parameters.** The light curves of SN 2018aoz (Supplementary Fig. 3) display two post-peak decay timescales, consistent with SNe powered by  $^{56}\text{Ni}$  and  $^{56}\text{Co}$  radioactive decay. As typically found in normal type Ia SNe, each of the near-infrared  $iJHK$ -band light curves reaches a primary peak before the  $B$  and  $V$  bands, followed by a secondary peak associated with the recombination of iron group elements in the ejecta<sup>49</sup>. The light curves of normal type Ia SNe in the photospheric phase from  $-10$  to 15 days since peak are also known to form a family of functions parameterized by the Phillips parameter,  $\Delta M_{15}(B)$ , which measures the post-peak decline rate in the  $B$ -band light curve<sup>90</sup>. To effectively include some peculiar type Ia SNe, such as the rapidly evolving 91bg-like subtype, the colour stretch parameter,  $s_{BV}$ , has been used as an alternative to  $\Delta M_{15}(B)$ ; it is defined by  $s_{BV} = t_{BV}/(30 \text{ days})$ , where  $t_{BV}$  is the time from the  $B$ -band peak to the maximum post-peak  $B - V$  colour<sup>91</sup>. We used SNooPy<sup>92</sup> to fit the  $BgVri$ -band light curves of SN 2018aoz with a normal type Ia SN template based on ref. 93, where the fitted parameters are stretch, time of  $B$ -band peak ( $t_p$ ) and DM. In the fitting process, we applied  $K$ -correction between the observer and rest-frame filter response functions for each filter (see below) and corrected for Galactic extinction. The best-fit template (Supplementary Fig. 3) provides a good comparison to our observed light curves with  $t_p$  and DM of  $58222.27 \pm 0.02$  (MJD) and  $31.75 \pm 0.08$  mag, respectively. The stretch parameter of the best-fit template is  $0.87 \pm 0.03$ .

We derive rest-frame magnitudes for SN 2018aoz by adopting the DM and  $K$ -corrections from the best-fit template and Galactic extinction correction. The  $K$ -corrections are insubstantial ( $< 0.02$  mag) given the relatively small redshift of the SN. With rest-frame light curves for the SN and with polynomial fitting, we measured the peak absolute magnitudes of each  $BVi$ -band light curve to be  $-19.319 \pm 0.009$  mag,  $-19.226 \pm 0.009$  mag and  $-18.614 \pm 0.012$  mag, respectively. The corrected  $BVi$ -band light curves each attained their peaks at  $-0.86$  days,  $-0.97$  days and  $-3.98$  days (in the observer frame) prior to  $t_p$  obtained from the above template fitting, respectively. We also measured the Phillips parameter and colour stretch parameter to be  $\Delta M_{15}(B) = 1.117 \pm 0.015$  mag and  $s_{BV} = 0.797 \pm 0.019$ , respectively. These parameters are close to the average of normal type Ia SNe<sup>32,91</sup>, whereas they are inconsistent with subluminal (91bg-like) and overluminous (91T-like) events, confirming the classification of SN 2018aoz as a normal type Ia SN.

## Data availability

Source data for Fig. 1 during 0–1 days since first light are provided with this paper, whereas data for the entire single-epoch ultraviolet to near-infrared light curves are provided in the Supplementary Information. All photometric and spectroscopic data are also available on the Open Supernova Catalog<sup>70</sup> and WISEREP3<sup>75</sup>. The modelled light curves and spectra of our He-shell DDet simulations are available at <https://github.com/niyuanqi/he-shell-ddet>.

## Code availability

We performed light curve template fitting in the post-infant phase using SNooPy, available at <https://csp.obs.carnegiescience.edu/data/snpy/snpy>. In our He-shell DDet models, hydrodynamics and nucleosynthesis simulations were conducted using Castro<sup>94,95</sup> and the radiative transfer calculations were conducted using

Sedona<sup>86</sup>. The code used to measure the KMTNet light curves of SN 2018aoz, construct the bolometric light curves and generate the analytic  $^{56}\text{Ni}$ -powered light curve models are available at <https://github.com/niyuanqi/SNAP>. IRAF is distributed by the National Optical Astronomy Observatory, which is operated by the Association of Universities for Research in Astronomy, Inc., under cooperative agreement with the National Science Foundation.

Received: 17 August 2021; Accepted: 6 January 2022;  
Published online: 17 February 2022

## References

- Matteucci, F. *Chemical Evolution of Galaxies* (Springer, 2012).
- Riess, A. G. et al. Observational evidence from supernovae for an accelerating Universe and a cosmological constant. *Astron. J.* **116**, 1009–1038 (1998).
- Perlmutter, S. et al. Measurements of  $\Omega$  and  $\Lambda$  from 42 high-redshift supernovae. *Astrophys. J.* **517**, 565–586 (1999).
- Maoz, D., Mannucci, F. & Nelemans, G. Observational clues to the progenitors of type Ia supernovae. *Annu. Rev. Astron. Astrophys.* **52**, 107–170 (2014).
- Blondin, S. et al. The spectroscopic diversity of type Ia supernovae. *Astron. J.* **143**, 126 (2012).
- Polin, A., Nugent, P. & Kasen, D. Observational predictions for sub-Chandrasekhar mass explosions: further evidence for multiple progenitor systems for type Ia supernovae. *Astrophys. J.* **873**, 84 (2019).
- Townsley, D. M., Miles, B. J., Shen, K. J. & Kasen, D. Double detonations with thin, modestly enriched helium layers can make normal type Ia supernovae. *Astrophys. J. Lett.* **878**, L38 (2019).
- Shen, K. J. et al. Non-local thermodynamic equilibrium radiative transfer simulations of sub-Chandrasekhar-mass white dwarf detonations. *Astrophys. J. Lett.* **909**, L18 (2021).
- Reinecke, M., Hillebrandt, W. & Niemeyer, J. C. Three-dimensional simulations of type Ia supernovae. *Astron. Astrophys.* **391**, 1167–1172 (2002).
- Maeda, K., Jiang, J.-A., Shigeyama, T. & Doi, M. Type Ia supernovae in the first few days: signatures of helium detonation versus interaction. *Astrophys. J.* **861**, 78 (2018).
- Jiang, J.-A. et al. A hybrid type Ia supernova with an early flash triggered by helium-shell detonation. *Nature* **550**, 80–83 (2017).
- De, K. et al. ZTF 18aaqaesu (SN2018byg): a massive helium-shell double detonation on a sub-Chandrasekhar-mass white dwarf. *Astrophys. J. Lett.* **873**, L18 (2019).
- Bulla, M. et al. ZTF early observations of type Ia supernovae. III. Early-time colors as a test for explosion models and multiple populations. *Astrophys. J.* **902**, 48 (2020).
- Marion, G. H. et al. SN 2012cg: evidence for interaction between a normal SN Ia and a non-degenerate binary companion. *Astrophys. J.* **820**, 92 (2016).
- Hosseinzadeh, G. et al. Early blue excess from the type Ia supernova 2017cbv and implications for its progenitor. *Astrophys. J. Lett.* **845**, L11 (2017).
- Shappee, B. J. et al. Strong evidence against a non-degenerate companion in SN 2012cg. *Astrophys. J.* **855**, 6 (2018).
- Dimitriadis, G. et al. K2 observations of SN 2018oh reveal a two-component rising light curve for a type Ia supernova. *Astrophys. J. Lett.* **870**, L1 (2019).
- Jiang, J.-A., Doi, M., Maeda, K. & Shigeyama, T. Surface radioactivity or interactions? Multiple origins of early-excess type Ia supernovae and associated subclasses. *Astrophys. J.* **865**, 149 (2018).
- Stritzinger, M. D. et al. Red versus blue: early observations of thermonuclear supernovae reveal two distinct populations? *Astrophys. J. Lett.* **864**, L35 (2018).
- Sand, D. J. et al. Nebular spectroscopy of the “blue bump” type Ia supernova 2017cbv. *Astrophys. J.* **863**, 24 (2018).
- Nugent, P. E. et al. Supernova SN 2011fe from an exploding carbon–oxygen white dwarf star. *Nature* **480**, 344–347 (2011).
- Foley, R. J. et al. Very early ultraviolet and optical observations of the type Ia supernova 2009ig. *Astrophys. J.* **744**, 38 (2012).
- Olling, R. P. et al. No signature of ejecta interaction with a stellar companion in three type Ia supernovae. *Nature* **521**, 332–335 (2015).
- Cartier, R. et al. Early observations of the nearby type Ia supernova SN 2015F. *Mon. Not. R. Astron. Soc.* **464**, 4476–4494 (2017).
- Holmbo, S. et al. Discovery and progenitor constraints on the type Ia supernova 2013gy. *Astron. Astrophys.* **627**, A174 (2019).
- Miller, A. A. et al. ZTF early observations of type Ia supernovae. II. First light, the initial rise, and time to reach maximum brightness. *Astrophys. J.* **902**, 47 (2020).
- Moon, D.-S. et al. Supernova and optical transient observations using the three wide-field telescope array of the KMTNet. *Proc. SPIE* **9906**, 99064I (2016).
- Kim, S.-L. et al. KMTNET: a network of 1.6 m wide-field optical telescopes installed at three southern observatories. *J. Korean Astron. Soc.* **49**, 37–44 (2016).
- Norris, M. A. & Kannappan, S. J. The ubiquity and dual nature of ultra-compact dwarfs. *Mon. Not. R. Astron. Soc.* **414**, 739–758 (2011).

30. Tartaglia, L. et al. The early detection and follow-up of the highly obscured type II supernova 2016ija/DLT16am. *Astrophys. J.* **853**, 62 (2018).
31. Brown, T. M. et al. Las Cumbres Observatory Global Telescope network. *Publ. Astron. Soc. Pac.* **125**, 1031 (2013).
32. Parrent, J., Friesen, B. & Parthasarathy, M. A review of type Ia supernova spectra. *Astrophys. Space Sci.* **351**, 1–52 (2014).
33. Pereira, R. et al. Spectrophotometric time series of SN 2011fe from the Nearby Supernova Factory. *Astron. Astrophys.* **554**, A27 (2013).
34. Li, W. et al. Photometric and spectroscopic properties of type Ia supernova 2018oh with early excess emission from the Kepler 2 observations. *Astrophys. J.* **870**, 12 (2019).
35. Goobar, A. et al. Constraints on the origin of the first light from SN 2014J. *Astrophys. J.* **799**, 106 (2015).
36. Piro, A. L. & Nakar, E. What can we learn from the rising light curves of radioactively powered supernovae? *Astrophys. J.* **769**, 67 (2013).
37. Piro, A. L. & Nakar, E. Constraints on shallow  $^{56}\text{Ni}$  from the early light curves of type Ia supernovae. *Astrophys. J.* **784**, 85 (2014).
38. Pinto, P. A. & Eastman, R. G. The physics of type IA supernova light curves. II. Opacity and diffusion. *Astrophys. J.* **530**, 757–776 (2000).
39. Kasen, D. Seeing the collision of a supernova with its companion star. *Astrophys. J.* **708**, 1025–1031 (2010).
40. Piro, A. L., Chang, P. & Weinberg, N. N. Shock breakout from type Ia supernova. *Astrophys. J.* **708**, 598–604 (2010).
41. Mihalas, D. Statistical-equilibrium model atmospheres for early-type stars. I. Hydrogen continua. *Astrophys. J.* **149**, 169 (1967).
42. Mihalas, D. & Stone, M. E. Statistical equilibrium model atmospheres for early-type stars. III. Hydrogen and helium continua. *Astrophys. J.* **151**, 293–310 (1968).
43. Magee, M. R. et al. Determining the  $^{56}\text{Ni}$  distribution of type Ia supernovae from observations within days of explosion. *Astron. Astrophys.* **634**, A37 (2010).
44. Nomoto, K. & Leung, S.-C. in *Handbook of Supernovae* (eds Alsabti, A. W. & Murdin, P.) 1275–1313 (Springer, 2017).
45. Maeda, K. et al. Nucleosynthesis in two-dimensional delayed detonation models of type Ia supernova explosions. *Astrophys. J.* **712**, 624–638 (2010).
46. Seitzzahl, I. R. et al. Three-dimensional delayed-detonation models with nucleosynthesis for type Ia supernovae. *Mon. Not. R. Astron. Soc.* **429**, 1156–1172 (2013).
47. Seitzzahl, I. R. et al. Three-dimensional simulations of gravitationally confined detonations compared to observations of SN 1991T. *Astron. Astrophys.* **592**, A57 (2016).
48. Shen, K. J. & Moore, K. The initiation and propagation of helium detonations in white dwarf envelopes. *Astrophys. J.* **797**, 46 (2014).
49. Kasen, D. Secondary maximum in the near-infrared light curves of type Ia supernovae. *Astrophys. J.* **649**, 939–953 (2006).
50. Han, X. et al. SN 2017cfd: a normal type Ia supernova discovered very young. *Astrophys. J.* **892**, 142 (2020).
51. Maguire, K. et al. Exploring the spectral diversity of low-redshift type Ia supernovae using the Palomar Transient Factory. *Mon. Not. R. Astron. Soc.* **444**, 3258–3274 (2014).
52. Afsariardchi, N. et al. KSP-SN-2016kfk: a long-rising H-rich type II supernova with unusually high  $^{56}\text{Ni}$  mass discovered in the KMTNet Supernova Program. *Astrophys. J.* **881**, 22 (2019).
53. Moon, D.-S. et al. Rapidly declining hostless type Ia supernova KSP-OT-201509b from the KMTNet Supernova Program: transitional nature and constraint on  $^{56}\text{Ni}$  distribution and progenitor type. *Astrophys. J.* **910**, 151 (2021).
54. Reichart, D. et al. PROMPT: Panchromatic Robotic Optical Monitoring and Polarimetry Telescopes. *II Nuovo Cimento C* **28**, 767–770 (2005).
55. Valenti, S., Sand, D. J. & Wyatt, S. *DLT40 Transient Discovery Report for 2018-04-02*. Transient Name Server Discovery Report No. 2018-428 (IAU, 2018).
56. Brown, P. & Sand, D. *Swift UVOT Observations Show SN Ia 2018aoz/DLT18q Is UV-bright*. The Astronomer's Telegram No. 11511 (NASA, 2018).
57. Gehrels, N. et al. The Swift gamma-ray burst mission. *Astrophys. J.* **611**, 1005–1020 (2004).
58. Roming, P. W. A. et al. The Swift Ultra-Violet/Optical Telescope. *Space Sci. Rev.* **120**, 95–142 (2005).
59. DePoy, D. L. et al. A novel double imaging camera (ANDICAM). *Proc. SPIE* **4841**, 827–838 (2003).
60. Moffat, A. F. J. A theoretical investigation of focal stellar images in the photographic emulsion and application to photographic photometry. *Astron. Astrophys.* **3**, 455 (1969).
61. Trujillo, I., Aguerri, J. A. L., Cepa, J. & Gutiérrez, C. M. The effects of seeing on Sérsic profiles – II. The Moffat PSF. *Mon. Not. R. Astron. Soc.* **328**, 977–985 (2001).
62. Henden, A. A. et al. APASS Data Release 10. *AAS Meet. Abst.* **232**, 223.06 (2018).
63. Park, H. S. et al. Dwarf galaxy discoveries from the KMTNet Supernova Program. I. The NGC 2784 galaxy group. *Astrophys. J.* **848**, 19 (2017).
64. Stritzinger, M. et al. Optical photometry of the type Ia supernova 1999ee and the type Ib/c supernova 1999ex in IC 5179. *Astron. J.* **124**, 2100–2117 (2002).
65. Valenti, S. et al. The diversity of type II supernova versus the similarity in their progenitors. *Mon. Not. R. Astron. Soc.* **459**, 3939–3962 (2016).
66. Brown, P. J., Breeveld, A. A., Holland, S., Kuin, P. & Pritchard, T. SOUSA: the Swift Optical/Ultraviolet Supernova Archive. *Astrophys. Space Sci.* **354**, 89–96 (2014).
67. Breeveld, A. A. et al. An updated ultraviolet calibration for the Swift/UVOT. *AIP Conf. Ser.* **1358**, 373–376 (2011).
68. Breeveld, A. A. *SWIFT-UVOT-CALDB-15-06: Sensitivity Loss* [https://heasarc.gsfc.nasa.gov/docs/heasarc/caldb/swift/docs/uvot/uvotcaldb\\_throughput\\_06.pdf](https://heasarc.gsfc.nasa.gov/docs/heasarc/caldb/swift/docs/uvot/uvotcaldb_throughput_06.pdf) (2020).
69. Skrutskie, M. F. et al. The Two Micron All Sky Survey (2MASS). *Astron. J.* **131**, 1163–1183 (2006).
70. Guillochon, J., Parrent, J., Kelley, L. Z. & Margutti, R. An open catalog for supernova data. *Astrophys. J.* **835**, 64 (2017).
71. Jeong, W.-S. et al. Optical survey with KMTNet for dusty star-forming galaxies in the Akari Deep Field South. *J. Korean Astron. Soc.* **49**, 225–232 (2016).
72. Hook, I. M. et al. The Gemini-North Multi-Object Spectrograph: performance in imaging, long-slit, and multi-object spectroscopic modes. *Publ. Astron. Soc. Pac.* **116**, 425–440 (2004).
73. Schmidt, G. D., Weymann, R. J. & Foltz, C. B. A moderate-resolution, high-throughput CCD channel for the MMT spectrograph. *Publ. Astron. Soc. Pac.* **101**, 713–724 (1989).
74. Matheson, T. et al. Optical spectroscopy of type Ia supernovae. *Astron. J.* **135**, 1598–1615 (2008).
75. Yaron, O. & Gal-Yam, A. WISEREP—an interactive supernova data repository. *Publ. Astron. Soc. Pac.* **124**, 668–681 (2012).
76. Meikle, W. P. S. et al. An early-time infrared and optical study of the type Ia supernovae SN 1994D and 1991T. *Mon. Not. R. Astron. Soc.* **281**, 263–280 (1996).
77. Pignata, G. et al. Optical and infrared observations of SN 2002dj: some possible common properties of fast-expanding type Ia supernovae. *Mon. Not. R. Astron. Soc.* **388**, 971–990 (2008).
78. Blondin, S. & Tonry, J. L. Determining the type, redshift, and age of a supernova spectrum. *Astrophys. J.* **666**, 1024–1047 (2007).
79. Steer, I. et al. Redshift-independent distances in the NASA/IPAC Extragalactic Database: methodology, content, and use of NED-D. *Astron. J.* **153**, 37 (2017).
80. Riess, A. G. et al. A 2.4% determination of the local value of the Hubble constant. *Astrophys. J.* **826**, 56 (2016).
81. Mould, J. R. et al. The Hubble Space Telescope Key Project on the extragalactic distance scale. XXVIII. Combining the constraints on the Hubble constant. *Astrophys. J.* **529**, 786–794 (2000).
82. Tully, R. B. et al. Cosmicflows-2: the data. *Astron. J.* **146**, 86 (2013).
83. Schlafly, E. F. & Finkbeiner, D. P. Measuring reddening with Sloan Digital Sky Survey stellar spectra and recalibrating SFD. *Astrophys. J.* **737**, 103 (2011).
84. Fitzpatrick, E. L. Correcting for the effects of interstellar extinction. *Publ. Astron. Soc. Pac.* **111**, 63–75 (1999).
85. Fitzpatrick, E. L. & Massa, D. An analysis of the shapes of interstellar extinction curves. V. The IR-through-UV curve morphology. *Astrophys. J.* **663**, 320–341 (2007).
86. Poznanski, D., Prochaska, J. X. & Bloom, J. S. An empirical relation between sodium absorption and dust extinction. *Mon. Not. R. Astron. Soc.* **426**, 1465–1474 (2012).
87. Misgeld, I. & Hilker, M. Families of dynamically hot stellar systems over 10 orders of magnitude in mass. *Mon. Not. R. Astron. Soc.* **414**, 3699–3710 (2011).
88. Gavazzi, G., Fumagalli, M., Cucciati, O. & Boselli, A. A snapshot on galaxy evolution occurring in the Great Wall: the role of Nurture at  $z=0$ . *Astron. Astrophys.* **517**, A73 (2010).
89. Harris, W. E., Allwright, J. W. B., Pritchard, C. J. & van den Bergh, S. The luminosity distribution of globular clusters in three giant Virgo ellipticals. *Astrophys. J. Suppl.* **76**, 115–151 (1991).
90. Phillips, M. M. et al. The reddening-free decline rate versus luminosity relationship for type Ia supernovae. *Astron. J.* **118**, 1766–1776 (1999).
91. Burns, C. R. et al. The Carnegie Supernova Project: intrinsic colors of type Ia supernovae. *Astrophys. J.* **789**, 32 (2014).
92. Burns, C. R. et al. The Carnegie Supernova Project: light-curve fitting with SNooPy. *Astron. J.* **141**, 19 (2011).
93. Hsiao, E. Y. et al.  $K$ -corrections and spectral templates of type Ia supernovae. *Astrophys. J.* **663**, 1187–1200 (2007).
94. Almgren, A. S. et al. CASTRO: a new compressible astrophysical solver. I. Hydrodynamics and self-gravity. *Astrophys. J.* **715**, 1221–1238 (2010).
95. Zingale, M. et al. Meeting the challenges of modeling astrophysical thermonuclear explosions: Castro, Maestro, and the AMReX astrophysics suite. *J. Phys. Conf. Ser.* **1031**, 012024 (2018).
96. Kasen, D., Thomas, R. C. & Nugent, P. Time-dependent Monte Carlo radiative transfer calculations for three-dimensional supernova spectra, light curves, and polarization. *Astrophys. J.* **651**, 366–380 (2006).

## Acknowledgements

This research has made use of the KMTNet system operated by the Korea Astronomy and Space Science Institute (KASI), and the data were obtained at the three host sites of CTIO in Chile, SAAO in South Africa and SSO in Australia. The Gemini South observations were obtained under the K-GMT Science Program (PID GS-2018A-Q-117 and GS-2018B-Q-121) of KASI. The Swift observations were triggered through the Swift GI program 80NSSC19K0316. SOUSA is supported by NASA's Astrophysics Data Analysis Program through grant no. NNX13AF35G. Some of the data presented here were obtained at the W. M. Keck Observatory, which is operated as a scientific partnership among the California Institute of Technology, the University of California and NASA. The Observatory was made possible by the generous financial support of the W. M. Keck Foundation. The Computational HEP program in the United States Department of Energy's Science Office of High Energy Physics provided simulation resources through grant no. KA2401022. This research used resources of the National Energy Research Scientific Computing Center, a Department of Energy Office of Science User Facility operated under contract no. DE-AC02-05CH11231. D.-S.M., M.R.D. and C.D.M. are supported by Discovery Grants from the Natural Sciences and Engineering Research Council of Canada. D.-S.M. was supported in part by a Leading Edge Fund from the Canadian Foundation for Innovation (project no. 30951). M.R.D. was supported in part by the Canada Research Chairs Program, the Canadian Institute for Advanced Research (CIFAR) and the Dunlap Institute at the University of Toronto. D.J.S. acknowledges support by NSF grant nos. AST-1821987, 1821967 and 1908972 and from the Heising-Simons Foundation under grant no. 2020-1864. S.G.-G. acknowledges support by FCT under project CRISP PTDC/FIS-AST-31546 and project UIDB/00099/2020. H.S.P. was supported in part by a National Research Foundation (NRF) of Korea grant funded by the Korean government (MSIT, Ministry of Science and ICT; no. NRF-2019R1F1A1058228). P.J.B. acknowledges support from the Swift GI program 80NSSC19K0316. S.V., Y.D. and K.A.B. acknowledge support by NSF grant nos. AST-1813176 and AST-2008108. C.M. acknowledges support by NSF grant AST-1313484. I.A. is a CIFAR Azrieli Global Scholar in the Gravity and the Extreme Universe Program and acknowledges support from that program, from the Israel Science Foundation (grant nos. 2108/18 and 2752/19), from the United States – Israel Binational Science Foundation (BSF) and from an Israeli Council for Higher Education Alon Fellowship. R.L.B. acknowledges support by NASA through Hubble Fellowship grant no. 51386.01 awarded by the Space Telescope Science Institute, which is operated by the Association of Universities for Research in Astronomy, Inc., for NASA under contract no. NAS 5-26555. A.G.-Y. acknowledges support from the European Union via ERC grant no. 725161, the ISF GW Excellence Center, an IMOS space infrastructure grant and BSF/Transformative and GIF grants, as well as from the Benozio Endowment Fund for the Advancement of Science, the Deloro Institute for Advanced Research in Space and Optics, the Veronika A. Rabl Physics Discretionary Fund, P. and T. Gardner, the Yeda-Sela Center for Basic Research and a WIS-CIT joint research grant. A.G.-Y. is the recipient of the Helen and Martin Kimmel Award for Innovative Investigation. L.G. acknowledges financial support from the Spanish Ministerio de Ciencia e Innovación (MCIN), the Agencia Estatal de Investigación (AEI) 10.13039/501100011033, the European

Social Fund (ESF) 'Investing in your future' under the 2019 Ramón y Cajal program RYC2019-027683-I and the PID2020-115253GA-I00 HOSTFLOWS project, as well as from the Centro Superior de Investigaciones Científicas (CSIC) under the PIE project 20215AT016. G.P. acknowledges support from the Millennium Science Initiative through grant no. IC120009. J.A. is supported by the Stavros Niarchos Foundation (SNF) and the Hellenic Foundation for Research and Innovation (HFRI) under the 2nd Call of 'Science and Society' Action 'Always strive for excellence – Theodoros Papazoglou' (project no. 01431).

## Author contributions

Y.Q.N. conducted most of the analyses under the supervision of D.-S.M. and M.R.D. D.-S.M. is the principal investigator of the KSP that detected the infant-phase features of SN 2018aoz and wrote the KSP pipeline. M.R.D. led the collaboration between the KSP and other partners. Y.Q.N., D.-S.M. and M.R.D. co-drafted the manuscript. A.P. conducted the He-shell DDet simulations under the supervision of P.N. D.-S.M., M.R.D., Y.Q.N., N.A., S.G.-G., S.C.K., Y.L., H.S.P., J.A., A.G.-Y., S.B.C., G.P. and S.D.R. are members of the KSP. N.A., D.-S.M., M.R.D., R.G.C. and C.D.M. are members of the Canadian Gemini South observing programme for the KSP. H.S.P., D.-S.M., S.C.K. and Y.L. are members of the Korean Gemini South observing programme for the KSP. A.L.P. performed the shock breakout modelling. P.J.B. led the Swift program for ultraviolet observations with help from S.B.C. L.G. and G.P. obtained the ANDICAM near-infrared observations. D.J.S. and S.V. co-led the DLT40 programme. J.H., D.E.R., V.K. and S.W. contributed to the operation of the DLT40 programme. S.Y. built the machine-learning implementation for the DLT40 survey. K.A.B., Y.D., J.E.A. and N.S. are members of the DLT40 team who obtained the Keck and MMT spectra. S.-M.C. and Y.L. helped operate the KMTNet. D.A.H., C.M., I.A., J.B., D.H. and G.H. contributed to the LCO photometry and the FLOYDS spectroscopy. M.R.D., R.L.B., T.W.-S.H., S.D.J., N.M. and J.R. contributed to the du Pont WFCCD and Magellan spectra. All of the authors contributed to the discussion.

## Competing interests

The authors declare no competing interests.

## Additional information

**Supplementary information** The online version contains supplementary material available at <https://doi.org/10.1038/s41550-022-01603-4>.

**Correspondence and requests for materials** should be addressed to Dae-Sik Moon.

**Peer review information** *Nature Astronomy* thanks Ji-an Jiang and the other, anonymous, reviewer(s) for their contribution to the peer review of this work.

**Reprints and permissions information** is available at [www.nature.com/reprints](http://www.nature.com/reprints).

**Publisher's note** Springer Nature remains neutral with regard to jurisdictional claims in published maps and institutional affiliations.

© The Author(s), under exclusive licence to Springer Nature Limited 2022

<sup>1</sup>David A. Dunlap Department of Astronomy and Astrophysics, University of Toronto, Toronto, Ontario, Canada. <sup>2</sup>The Observatories of the Carnegie Institution for Science, Pasadena, CA, USA. <sup>3</sup>TAPIR, Walter Burke Institute for Theoretical Physics, Caltech, Pasadena, CA, USA. <sup>4</sup>Steward Observatory, Department of Astronomy, University of Arizona, Tucson, AZ, USA. <sup>5</sup>CENTRA-Centro de Astrofísica e Gravitação and Departamento de Física, Instituto Superior Técnico, Universidade de Lisboa, Lisboa, Portugal. <sup>6</sup>Korea Astronomy and Space Science Institute, Daejeon, Republic of Korea. <sup>7</sup>Korea University of Science and Technology, Daejeon, Republic of Korea. <sup>8</sup>Department of Astronomy and Space Science, Chungnam National University, Daejeon, Republic of Korea. <sup>9</sup>Department of Physics, University of California, Santa Barbara, CA, USA. <sup>10</sup>Las Cumbres Observatory, Goleta, CA, USA. <sup>11</sup>Department of Astronomy, University of California, Berkeley, CA, USA. <sup>12</sup>Lawrence Berkeley National Laboratory, Berkeley, CA, USA. <sup>13</sup>Department of Physics and Astronomy, Texas A&M University, College Station, TX, USA. <sup>14</sup>George P. and Cynthia Woods Mitchell Institute for Fundamental Physics & Astronomy, College Station, TX, USA. <sup>15</sup>Institute of Space Sciences (ICE-CSIC), Universitat Autònoma de Barcelona, Barcelona, Spain. <sup>16</sup>Institut d'Estudis Espacials de Catalunya (IEEC), Barcelona, Spain. <sup>17</sup>Center for Astrophysics | Harvard & Smithsonian, Cambridge, MA, USA. <sup>18</sup>The NSF AI Institute for Artificial Intelligence and Fundamental Interactions, Cambridge, MA, USA. <sup>19</sup>Department of Physics and Astronomy, University of California, Davis, CA, USA. <sup>20</sup>Institute of Astrophysics, FORTH, Department of Physics, University of Crete, Heraklion, Greece. <sup>21</sup>Max-Planck-Institut für Radioastronomie, Bonn, Germany. <sup>22</sup>Argelander Institut für Astronomie, Bonn, Germany. <sup>23</sup>The School of Physics and Astronomy, Tel Aviv University, Tel Aviv, Israel. <sup>24</sup>Canadian Institute for Advanced Research (CIFAR), Toronto, Ontario, Canada. <sup>25</sup>Department of Astrophysical Sciences, Princeton University, Princeton, NJ, USA. <sup>26</sup>DIRAC Institute, Department of Astronomy, University of Washington, Seattle, WA, USA. <sup>27</sup>Astrophysics Science Division, NASA Goddard Space Flight Center, Greenbelt, MD, USA. <sup>28</sup>Joint Space-Science Institute, University of Maryland, College Park, MD, USA. <sup>29</sup>School of Space Research, Kyung Hee University, Yongin, Republic of Korea. <sup>30</sup>Department of Particle Physics and Astrophysics, Weizmann Institute of Science, Rehovot, Israel. <sup>31</sup>Department of Physics and Astronomy, University of North Carolina at Chapel Hill, Chapel Hill, NC, USA. <sup>32</sup>Central (Pulkovo) Observatory of Russian Academy of Sciences, Saint Petersburg, Russia. <sup>33</sup>Las Campanas Observatory, Carnegie Observatories, La Serena, Chile. <sup>34</sup>Departamento de Ciencias Físicas, Universidad Andres Bello, Santiago, Chile. <sup>35</sup>Millennium Institute of Astrophysics (MAS), Santiago, Chile. <sup>36</sup>Department of Physics and Astronomy, Macquarie University, Sydney, New South Wales, Australia. <sup>37</sup>Macquarie University Research Centre for Astronomy, Astrophysics and Astrophotonics, Sydney, New South Wales, Australia. <sup>38</sup>The Oskar Klein Centre, Department of Astronomy, Stockholm University, Stockholm, Sweden. <sup>39</sup>Hubble Fellow: Rachael L. Beaton. <sup>40</sup>Carnegie-Princeton Fellow: Rachael L. Beaton. ✉e-mail: [moon@astro.utoronto.ca](mailto:moon@astro.utoronto.ca)